Applied Catalysis B: Environmental 254 (2019) 601–611

Contents lists available at ScienceDirect

Applied Catalysis B: Environmental

journal homepage: www.elsevier.com/locate/apcatb

Iron-nitrogen-carbon species for oxygen electro-reduction and Zn-air battery: Surface engineering and experimental probe into active sites

Anquan Zhu, Lulu Qiao, Pengfei Tan, Yongjin Ma, Weixuan Zeng, Rui Dong, Cheng Ma, Jun Pan*

State Key Laboratory for Powder Metallurgy, Central South University, Changsha 410083, PR China

ARTICLE INFO

Keywords:
Oxygen reduction reaction
Active sites
Porous structures
Iron-nitrogen-carbon
Zn-air battery

ABSTRACT

It still requires further investigations on the status of iron-based compounds and actual active sites in iron and nitrogen modified carbon based oxygen reduction catalysts (Fe—N—C), even though Fe-N_x groups have been confirmed as a type of dominating active site for most Fe—N—C systems. Herein, a facile and practical surface engineering process is adopted to transform metallic iron and iron trioxide nanoparticles into Fe_2N nanocrystals, meanwhile to make their coated graphitic carbon shells interrupted and broken. This sufficiently facilitates the elimination of embedded Fe_2N with a subsequent acid-etching process, eventually obtaining AA-Fe_2N@NC sample. Based on various physicochemical characterizations, it is found that the relative concentrations of defective carbon and pyridinic N for AA-Fe_2N@NC are clearly enhanced, compared to its counterpart (Fe_2N@NC sample). Electrochemical measurements demonstrate that AA-Fe_2N@NC instead of Fe_2N@NC has optimal onset potential (72 mV positive shift), half-wave potential (45 mV positive shift) and limiting current density values (increased by 0.97 mA cm^{-2}). When used as an air cathode of rechargeable Zn-air battery, it delivers a high power density of 168.15 mW cm^{-2}, meanwhile a long-life cycling durability (60 h operation with an increased voltage gap of only 70 mV) is realized at 5 mA cm^{-2}. Combined with the calculation of TOF values and SCN^- inhibition test, we make a conclusion and highlight that, in alkaline electrolyte, carbon defects and pyridinic N for this Fe—N—C system rather than Fe_2N compounds or Fe-N_x groups actually serve as the dominant active sites to afford a high-performance output of ORR activity.

1. Introduction

In consideration of their desirable features including competitive activities, reliable durability, robust methanol immunity and low cost, nitrogen doped carbon (N-C) and transition metal iron and nitrogen modified carbon (Fe—N—C) have been more and more investigated as alternatives of noble metal Pt or Pt-based alloys to serve as oxygen reduction reaction (ORR) electrodes in sustainable energy conversion devices, including metal-air batteries, fuel cells and water splitting reactors [1–5]. With these green and renewable energy conversion and storage techniques, a suite of energy and environment problems caused by the excessive consumption of fossil fuels will be effectually alleviated and even hopeful to be solved [6]. In order to achieve this sustainable development of our society, one of the key issues we currently faced with is to design and produce the above-mentioned carbon-based electrocatalysts with remarkable activity and stability [7]. But unfortunately, researchers devoting to develop these carbonaceous matrixes, especially Fe—N—C catalysts containing Fe-based compounds, with satisfactory catalytic properties have not yet reach a consensus about the active site debates until now [2–4,8]. This calls for more valuable researches to distinguish the real active sites catalyzing for high-efficiency ORR and Zn-air battery based on Fe—N—C category electrodes [9].

For nitrogen doped carbon catalysts, both experimental and theoretical studies have confirmed the positive effect of nitrogen doping on ORR performances [10,11]. After implanting nitrogen atoms into carbon skeletons, there are four types of nitrogen atoms, denoted as pyridinic N, pyrrolic N, graphitic N and oxidized N, respectively, existing in N—C species [12,13]. Among them, pyridinic N and graphitic N are accepted by different researchers as prime active site to determine the ORR activities [10], of which the former is generally preferred [11]. It is believed that carbon atoms adjacent to doping sites would have large positive charge density because of the high electronegativity and strong electron affinity ability of nitrogen atoms. Pyridinic N can be favorable for the adsorption of O_2 molecule while graphitic N is capable of facilitating the breakage of O—O bonds, consequently providing a much enhanced ORR activity [4,14]

If iron atom is linked with nitrogen atoms to form Fe-N_x groups, the

* Corresponding author.
E-mail address: jun.pan@csu.edu.cn (J. Pan).

https://doi.org/10.1016/j.apcatb.2019.05.037
Received 5 November 2018; Received in revised form 4 April 2019; Accepted 9 May 2019
Available online 14 May 2019
0926-3373/ © 2019 Elsevier B.V. All rights reserved.

active components of Fe—N—C electrocatalysts are much more complicated. For this kind of catalysts, Fe atoms are prone to coordinating with pyridinic N and then generate Fe-N_x moieties, which have been identified as a kind of key active site for ORR in both acidic and alkaline electrolytes [15,16]. Nevertheless, the formation of Fe-N_x groups is highly uncontrollable and depends intimately on the selection of precursors, the design of synthetic route and the control of reaction condition [1,17,18]. These aspects synergistically lead to the final forms of existing in as-obtained Fe—N—C catalysts, Fe-N_x groups, Fe-based nanoparticles (metallic iron, iron oxide, iron nitride, or others) or both co-existing [19]. Up to now, only a few reports have been involved with unveiling the real role of inorganic Fe-based compounds and how they promote or inhibit the ORR activity of Fe—N—C catalysts [20]. Therefore, it remains indistinct that these Fe-based nanoparticles acting as actual active sites or just bonding with nitrogen atoms to facilitate the production of other active sites.

With on doubt, it is of great significance to illustrate the active sites of Fe—N—C catalysts according to rational experimental investigations. As demonstrated by dozens of reports [2,21,22], graphitic carbon coated metallic iron and iron oxide nanoparticles cannot be removed entirely by mineral acid, which impedes the implement of exploration on the actual active sites. In this work, we, at first, developed a g-C_3N_4/$FeC_2O_4{\cdot}2H_2O$ intermediate from hydrothermal reaction of d-glucose, iron oxalate and g-C_3N_4 mixtures. After the thermolysis of g-C_3N_4/Fe-$C_2O_4{\cdot}2H_2O$ composite at argon atmosphere, graphitic carbon encapsulated metallic iron and iron oxide nanoparticles decorated nitrogen doped porous carbon (Fe_2O_3@NC) is fabricated. Through an ammonia treatment and acid-washing process, it is successful to transform metallic Fe and Fe_2O_3 particles into Fe_2N compounds and then getting rid of Fe_2N, eventually acquiring Fe_2N@NC sample and AA-Fe_2N@NC sample, respectively. This surface engineering process offers a prerequisite to gain insights into the actual active centers and the role of Fe_2N compound as well as Fe-N_x groups in as-synthesized Fe—N—C catalysts towards ORR. Combined with in-depth investigation on morphology, structure, composition and property of the Fe—N—C catalysts, it is advocated that plentiful carbon defects and pyridinic N actually are the primary active sites for ORR in alkaline electrolyte. We believe it could be helpful to exploit satisfactory Fe—N—C catalysts to meet the requirement of large-scale commercialization.

2. Experimental section

2.1. Synthesis of g-C_3N_4/$FeC_2O_4{\cdot}2H_2O$ precursor material

The porous g-C_3N_4 was pre-fabricated according to our previous reports [23]. After that, we aimed at preparing the g-C_3N_4/Fe-$C_2O_4{\cdot}2H_2O$ composites. In typical, d-glucose (2.16 g, AR, Xilong Chemical Co., Ltd. Guangzhou, China) was first dissolved into 30 mL deionized (DI) water. Then, 0.5 g as-obtained g-C_3N_4 and 0.36 g iron oxalate (AR, 99%, Aladdin Industrial Corporation Shanghai, China) were added into the above solution followed by sustaining an ultrasound bath for 1 h. When the g-C_3N_4 was dispersed uniformly, the whole reactive mixture was transferred to 50 mL Teflon autoclave and maintained at 160 °C for 10 h. To acquire the g-C_3N_4/$FeC_2O_4{\cdot}2H_2O$ composite, the hydrothermal precipitate need be centrifuged and washed with deionized water and ethanol for five times, in addition to dried overnight at 60 °C in a vacuum oven.

2.2. Synthesis of Fe_2O_3@NC and AA-Fe_2O_3@NC hybrids

Herein, the g-C_3N_4/$FeC_2O_4{\cdot}2H_2O$ composite was successfully fabricated as precursor material for the carbonization synthesis of Fe_2O_3@NC hybrids. To achieve our goal, as-prepared g-C_3N_4/$FeC_2O_4{\cdot}2H_2O$ composites (2 g) were annealed in argon at 800 °C for 1.5 h, in which the heating rate was 5 °C min^{-1}. After the reaction, the black powder (Fe_2O_3@NC hybrids) could be collected by centrifugation and washed with deionized water and ethanol. As a comparison, the Fe_2O_3@NC hybrids were subjected to an acid-activated process in 0.5 M H_2SO_4 solution for 24 h at room temperature. After centrifugation, washed and dried, as-obtained powder was denoted as AA-Fe_2O_3@NC sample.

2.3. Synthesis of Fe_2N@NC and AA-Fe_2N@NC hybrids

In an ammonia-treatment process, we succeed in converting Fe/Fe_2O_3 species into iron nitride (Fe_2N) species. Typically, the Fe_2O_3@NC hybrids (0.3 g) were poured into a crucible and then soaked in ammonia atmosphere. Other parameters (e.g. heating rate, reaction temperature, reaction time, flow rate and cooling rate) were identical to the above-mentioned synthetic process of Fe_2O_3@NC hybrids. The final product was named as Fe_2N@NC sample. Similar with AA-Fe_2O_3@NC sample, we obtained the AA-Fe_2N@NC after a facile acid-washing treatment of the Fe_2N@NC.

2.4. Electrochemical ORR measurements

All the electrochemical measurements were carried out by using a CHI 660E electrochemical workstation equipped with a rotating disk (Pine Rotating Disk Electrode, RDE) normal three-electrode system. A Pt wire served as the counter electrode, an Ag/AgCl in 3 M KCl as the reference electrode, a 0.1 M KOH solution as the electrolyte. In the process of cyclic voltammetry (CV) tests, the KOH electrolyte should be bubbled with N_2 or O_2 flow to achieve an oxygen-free or oxygen-saturated environment. For each working electrode test, 30 cycle CVs with a scan rate of 50 mV s^{-1} were accomplished to make it stable. Polarization curves (Linear Sweep Voltammetrys, LSVs) rotated between 400 and 2025 rpm were obtained under an uninterrupted O_2 flow, in which the sweep window and rate were 0.2 to −1 V vs. Ag/AgCl and 10 mV s^{-1}, respectively. The transferred electron number (n) can be calculated by the Koutechy − Levich (K − L) equation mentioned in previous reports [24]. The accelerated durability tests (ADT) were measured with a scan rate of 50 mV s^{-1} in O_2-saturated electrolyte, and the potential window was between 0.2 and −1 V vs. Ag/AgCl. Polarization curves before and after ADT tests were carried out to evaluate the stability of the samples. Methanol tolerance evaluation and SCN^- inhibition studies of the samples were performed in 0.1 M KOH electrolyte without or with the addition of 3 M methanol and 5 mM KSCN, similar with some published papers [25,26]

2.5. Assembly and measurement processes of Zn-air battery

Primary Zn-air battery was assembled by catalyst air cathode, Zn anode and electrolyte [27]. Herein, catalysts cathode was composed of three parts: gas diffusion layer (GDL), nickel foam (current collector) and catalytic layer (CL). Initially, commercial Ni foam should be rolled press and achieve a thickness of 0.1 mm. The GDL was made from a paste that was mixed by acetylene black and polytetrafluoroethylene emulsion (PTFE, 60 wt%) with a mass ratio of 3:7, In which the paste need be painted uniformly on pressed Ni foam and then continuously press the unit until its thickness reaches 0.45 mm. The CL was prepared by catalysts, acetylene black and PTFE emulsion in a weight ratio of 5:2:3. The combination of GDL, Ni foam and CL (air cathode) should be pressed to afford a total thickness of 0.4 mm, of which the CL had a working geometric area of 1 cm^2 and a loading density of 3 mg cm^{-2}. Finally, as-fabricated air cathode was maintained in a vacuum oven and dried at 200 °C for 1 h. In this battery system, a polished Zn plate (thickness of 0.3 mm) and a solution (6 M KOH and 0.2 M $Zn(Ac)_2$) were used as anode and electrolyte, respectively. As a comparison, the air cathode was also constructed from commercial Pt/C 20 wt% and RuO_2 (99.9%) of equal mass. For Zn-air battery test, the polarization curves were recorded by a CHI 660E electrochemical workstation with a scan rate of 5 mV s^{-1}. To evaluate the durability of Zn-air battery, the galvanostatic discharge and charge cycles (discharging for 10 min and

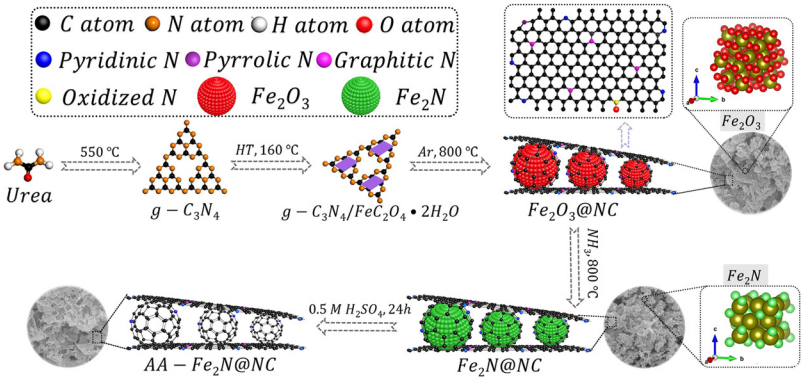

Scheme 1. Schematic illustration of synthesis processes for various Fe—N—C catalysts.

charging for 10 min at a constant current density of 5 mA cm^{-2}) were measured by a LANHE CT2001A battery testing system.

3. Results and discussion

3.1. Illustration of synthetic processes

The detailed synthetic illustration of diverse Fe—N—C samples is depicted in Scheme 1. As confirmed by previous reports [23,28], graphitic carbon nitride (g-C_3N_4), intrinsically possessing carbon, nitrogen element and porous structure, is generally deemed as promising precursor material to synthesize nitrogen-doped porous carbon. By means of a hydrothermal reaction of prefabricated g-C_3N_4, d-glucose and iron oxalate, the expansive surface of g-C_3N_4 could be bonded to a certain amount of amorphous carbon from the carbonization of d-glucose along with iron (II) oxalate dihydrate, in other words, the g-C_3N_4/Fe-C_2O_4·$2H_2O$ composite was successfully fabricated. This fact can be exactly determined by the X-ray diffraction (XRD) pattern and element mapping analysis. As shown in Fig. S1 (Supporting Information), both of g-C_3N_4 and g-C_3N_4/FeC_2O_4·$2H_2O$ composite have an obvious peak at 2θ ≈ 27.1° [29], which is indexed to the (002) plane of g-C_3N_4. However, a lot of additional peaks are observed in the XRD pattern of g-C_3N_4/FeC_2O_4·$2H_2O$ composite rather than that of g-C_3N_4, and these peaks are consistent with the standard card of FeC_2O_4·$2H_2O$ (JCPDS 23-0293), demonstrating the presence of FeC_2O_4·$2H_2O$ in the g-C_3N_4/Fe-C_2O_4·$2H_2O$ composite. In addition, the corresponding element mapping (Fig. S2, Supporting Information) also manifests the uniform distribution of C, N, Fe and O elements in the g-C_3N_4/FeC_2O_4·$2H_2O$ composite. To obtain the Fe_2O_3@NC sample, as-synthesized g-C_3N_4/FeC_2O_4·$2H_2O$ composite need to be maintained at 800 °C for 1.5 h under argon atmosphere. It is worth mentioning that the thermal decomposition and complicated reaction between amorphous carbon decorated g-C_3N_4 and FeC_2O_4·$2H_2O$ let a huge number of gases (including CO, CO_2, H_2O, and so on) out, which is responsible for the formation of defect sites and abundant pore structures. Defects are expected to serve as active sites for oxygen reduction reaction [30], meanwhile, plentiful pores are capable of accelerating diffusion of reactant gases and ions to the reaction active sites, in turn to enhance the output of ORR activity [31]. Along with these defect sites and pores in nitrogen doped carbon matrix might be formed in the processes of pyroreaction, there are a series of converting reactions related to Fe element as well. As we understand, iron trioxide and metallic Fe could be generated based on the following equations (Note: some oxygen might exist in the furnace tube):

$$FeC_2O_4 \cdot 2H_2O \xrightarrow{142\,^{\circ}C} FeC_2O_4 + 2H_2O \quad (1)$$

$$4\,FeC_2O_4 + O_2 \xrightarrow{\text{elevated temperature}} 2\,Fe_2O_3 + 4\,CO + 4CO_2 \quad (2)$$

$$Fe_2O_3 + CO + C \rightarrow 2\,Fe + 2\,CO_2 \quad (3)$$

As a result, Fe_2O_3 and metallic Fe nanoparticles embedded in nitrogen doped carbon (Fe_2O_3@NC) hybrids are produced. It has been proved that Fe_2O_3 and metallic Fe nanoparticles could not be removed completely by facile acid-washing if these particles are encompassed by graphitic carbon shell [22]. For iron nitride, however, it might be the other side of a coin. Therefore, the Fe_2O_3 and metallic Fe nanoparticles are converted as iron nitride (Fe_2N) nanoparticles through an ammonia treatment. Subsequently, as-fabricated Fe_2N@NC sample is immersed into 0.5 M sulfuric acid to wipe out the Fe_2N nanoparticles fixed in nitrogen doped carbon matrixes as much as possible, finally obtaining AA-Fe_2N@NC sample. Comparative research on the structures, components and properties of Fe_2N@NC and AA-Fe_2N@NC samples, it is enabled to better understand the real active sites of these Fe—N—C species.

3.2. Structure and composition characterization

To identify the phase compositions of as-obtained Fe—N—C species, XRD patterns were recorded and displayed in Fig. 1. For all samples, a broad and rough peak at 2θ ≈ 26.1° corresponds to the (002) plane of graphitic carbon [32], confirming the existence of graphitic carbon. In Fig. 1a, a set of peaks at 30.2°, 35.6°, 43.3°, 57.3° and 62.3° appear in the XRD patterns of Fe_2O_3@NC and AA-Fe_2O_3@NC samples, which are ascribed to the (200), (311), (400), (511) and (440) lattice planes of cubic Fe_2O_3 (JCPDS 39-1346) [33], respectively. Additionally, the sharp peak located at 44.7° is attributed to the (110) plane of cubic metallic Fe (JCPDS 87-0721), suggesting its good crystallinity. Comparatively speaking, this fact means that, even after acid-washing for 24 h, considerable metallic Fe and Fe_2O_3 nanoparticles still remain in the carbon matrix. After NH_3 treatment, metallic Fe and Fe_2O_3 particles are transformed into Fe_2N phases. The evidence is that apparent peaks at 37.4°, 40.6°, 42.7°, 56.4°, 67.1° and 75.4° are assigned to the (021), (200), (121), (221), (023) and (321) lattice planes of orthorhombic Fe_2N (JCPDS 50-0958) [34,35]. We fail to detect the trail of Fe_2N phase any more from the XRD pattern with a process of acid-washing, and speculate that the NH_3 activating treatment might create additional pore structures or defects in the graphitic carbon shell encapsulated Fe_2N cores. These pore structures or defects could facilitate the diffusion of H^+ ions into the inner of graphitic carbon shell, consequently eliminating Fe_2N nanoparticles. Hence, the peaks we can find in the XRD pattern (Fig. 1b) of AA-Fe_2N@NC are (002) and (100) plane of graphitic carbon, proving that acid-washing is an effective strategy to remove Fe_2N phases if embedded in broken graphitic carbon shells.

The morphology and microstructure of these Fe—N—C samples were probed by SEM and TEM techniques. As displayed in Fig. 2a-d and Fig. S3 (Supporting Information), it is revealed that Fe_2O_3@NC sample has a curly sheet-like structure loading with numerous graphitic carbon coated Fe/Fe_2O_3 nanoparticles, in which the average diameter of these nanoparticles are statistically evaluated to be about 24.5 nm. After

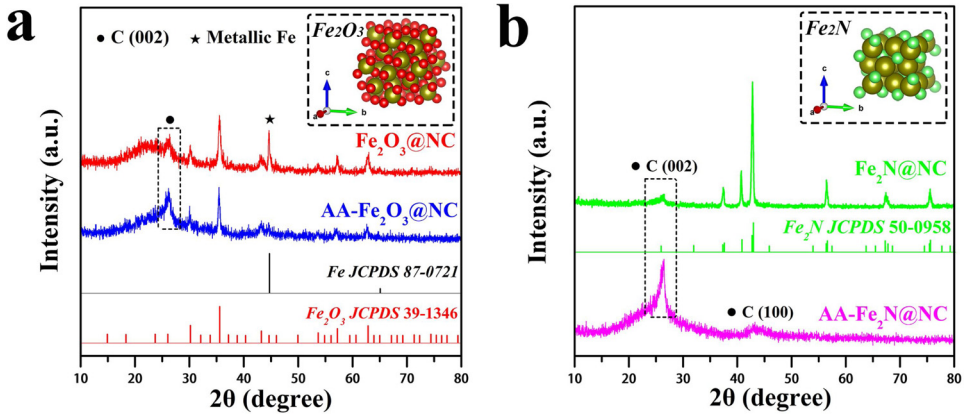

Fig. 1. XRD patterns of as-prepared Fe_2O_3@NC, AA-Fe_2O_3@NC, Fe_2N@NC and AA-Fe_2N@NC sample.

etching with H_2SO_4 solution, some metallic Fe and Fe_2O_3 particles are disappeared, but quite a lot of them are still reserved, which are consistent with the XRD result. Most worthy of mention is that we can clearly notice, for AA-Fe_2O_3@NC sample, more curved carbon flakes getting a chance to be exposed, in comparison to Fe_2O_3@NC sample. A SEM image of Fe_2N@NC sample is exhibited in Fig. 2e, revealing plenty of Fe_2N nanoparticles distributed uniformly in the curved nitrogen doped carbon plates, similar with Fe_2O_3@NC sample. Further observation (Fig. 2g) on the size of Fe_2N nanoparticles gives an average diameter of 28.5 nm, slightly bigger than that of Fe/Fe_2O_3 particles in Fe_2O_3@NC sample, implying an increased crystalline grain size caused by secondary heat-treatment. A high-resolution TEM (HRTEM) image of Fe_2N@NC sample is exhibited in Fig. 2h, of which few graphitic carbon layers (˜5 layers) encapsulated Fe_2N particles are visibly decorated on porous nitrogen doped carbon matrixes, and the distinct inter-planar spacings of 0.21 and 0.34 nm are related to the (121) plane of Fe_2N and (002) plane of graphitic carbon, respectively [34,36]. Taking a close look, it is observed that these graphitic carbon layers are interrupted and broken, which is definitely capable of facilitating the diffusion of H^+ to contact and react with inner Fe_2N cores, coinciding with our above conjecture. Moreover, the removal of Fe_2N particles could be also demonstrated by the disappearance of crystal diffraction spots in the selected area electron diffraction (SAED) patterns (inset of Fig. 2g and Fig. 2i), to some extent. It will contribute more active sites from the internal surfaces of graphitic carbon shell once these Fe_2N particles are out of original positions.

That is why a porous structure with more broken fringes or holes are detectable from the SEM (Fig. 2f) and TEM (Fig. 2i) images of AA-Fe_2N@NC sample. Fortunately, these broken fringes and holes of nitrogen doped carbon matrixes could not only provide a favorable mass transport pathway, but also form more carbon defects (Fig. 2j and Fig. 2k) as ORR active sites to enhance the catalytic activities [37]. Raman spectra is recognized as an effective tool to investigate the superficial defect structure of carbon-based materials [38]. Fig. 2m exhibits that the I_D/I_G ratio of AA-Fe_2N@NC sample (1.35) is much bigger than that of Fe_2N@NC sample (1.07), verifying a higher concentration defect carbon structures of AA-Fe_2N@NC sample, in line with the result of SEM and TEM observation [39,40]. These defects in AA-Fe_2N@NC sample are derived from the enhancement of surface area and pore volume on account of the elimination of Fe_2N nanoparticles. The

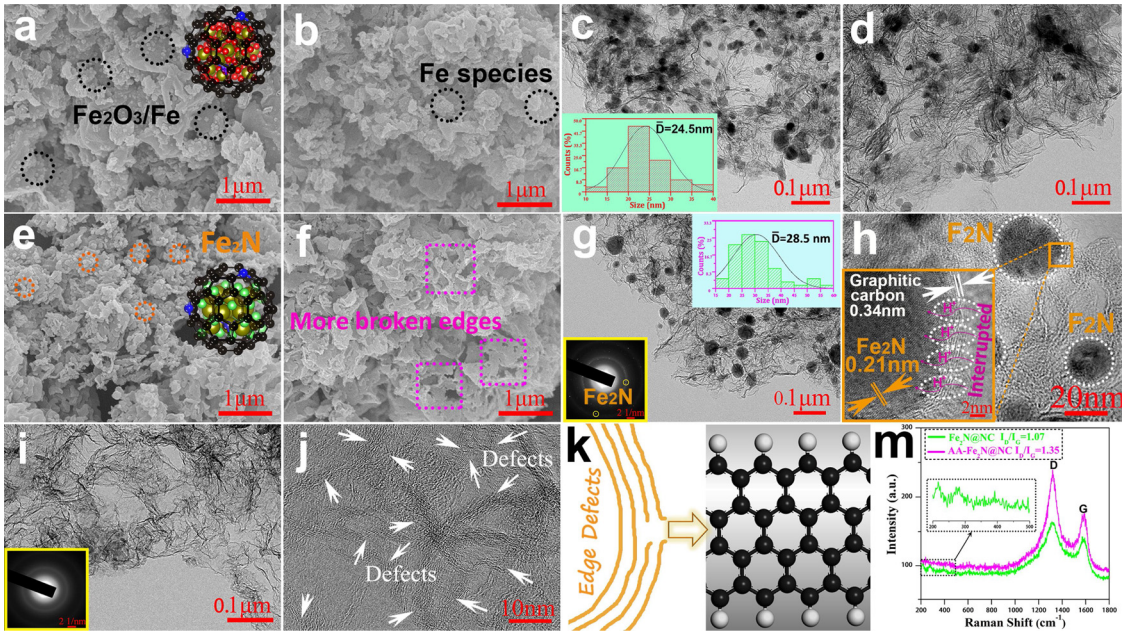

Fig. 2. SEM images of Fe_2O_3@NC (**a**), AA-Fe_2O_3@NC (**b**), Fe_2N@NC (**e**) and AA-Fe_2N@NC (**f**) sample. TEM images of Fe_2O_3@NC (**c**), AA-Fe_2O_3@NC (**d**),Fe_2N@NC (**g**) and AA-Fe_2N@NC (**i**) sample, inset of corresponding selective area electron diffraction pattern and an average diameter ($\bar{D}$) of Fe-based nanoparticles. HRTEM images of Fe_2N@NC (**h**) and AA-Fe_2N@NC (j) sample, inset of (**h**) is the enlarged view. Schematic illustration of edge defects in graphitic carbon (**k**). Raman spectrum of Fe_2N@NC and AA-Fe_2N@NC sample (**m**).

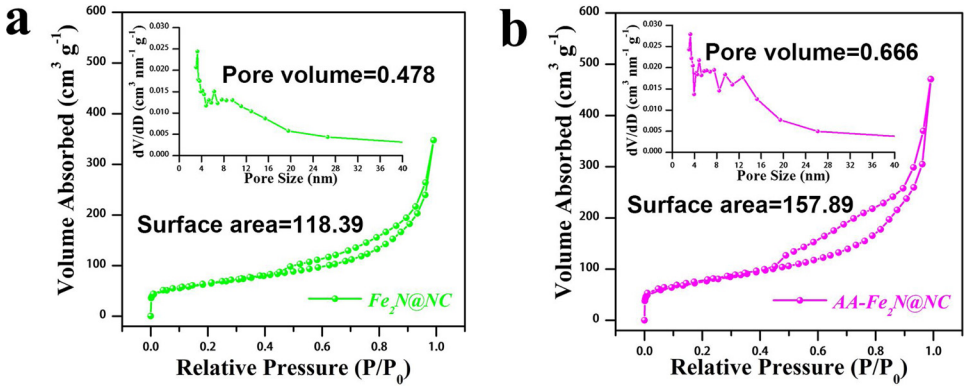

Fig. 3. N_2 adsorption–desorption isotherm and pore size distribution curves for Fe_2N@NC (**a**) and AA-Fe_2N@NC (**b**) sample.

elimination of Fe_2N particles can be also confirmed from the fact that several vibrating peaks around 200 cm^{-1} ~ 500 cm^{-1} for Fe_2N@NC sample, which is motivated by Fe_2N phase [41], are undetectable in the Raman spectra of AA-Fe_2N@NC sample, consistent with the above XRD and SEM/TEM analysis.

On the basis of morphology and microstructure analysis, nitrogen adsorption-desorption isotherm was employed to precisely explore the surface texture properties of samples. As shown in Fig. 3, both Fe_2N@NC and AA-Fe_2N@NC samples have typical IV isotherms, suggesting the coexistence of microporous and mesoporous structures [14,23,42]. Calculated by Brunauer–Emmett–Teller (BET) and Barrett-Joyner-Halenda (BJH) methods, the specific surface area and pore volume of Fe_2N@NC sample are 118.39 $m^2 g^{-1}$ and 0.478 $cm^3 g^{-1}$, respectively, slightly smaller than that of AA-Fe_2N@NC sample (157.89 $m^2 g^{-1}$ and 0.666 $cm^3 g^{-1}$). This means that surface area and pore volume will play similar roles in affecting the different catalytic activities of the two samples. It is discovered from the pore distribution curves that AA-Fe_2N@NC sample possesses a broader range of mesopore distribution. These pores serve as expedite pathways for migration of the molecules and ions and give rise to an enhanced mass transport ability, further leading to superior ORR activities. It is believed that the improved surface area and pore volume of AA-Fe_2N@NC sample result from the useful acid-washing treatment, in this process Fe_2N particles could be cleared off and more carbon structures are released. Similarly, this situation happens to Fe_2O_3@NC and AA-Fe_2O_3@NC samples (Fig. S5 and Table S1, Supporting Information). These carbon structures equipping with sufficient defects, testified by Raman spectra, could act as ORR active sites to strengthen electrocatalytic output.

The presence of C, N, O and Fe elements in Fe_2N@NC sample can be preliminarily affirmed by the corresponding energy dispersive spectra in Fig. S6 (Supporting Information), while the signal of Fe elements could hardly be collected from AA-Fe_2N@NC sample, indicating the absence of Fe_2N particles and rarely residual Fe element in carbon matrix after acid-washing treatment. To figure out the existence form and distribution of Fe elements, the HAADF-STEM image, the EDS linear spectra and STEM-EDS mapping spectra were characterized. As provided in Fig. 4a, the bright nanoparticles located in the main matrix are Fe_2N phases, which can be certified by the detailed distribution of Fe and N elements. Obviously, the intensive Fe signals are centralized at the Fe_2N particles, and these signals almost cannot be detected at the positions where no Fe_2N nanoparticles are resident. In addition, the EDS linear spectra (Fig. 4b and Fig. 4c) demonstrates that N elements distributes homogeneously across the line and overlaps with Fe elements. These reasonably make us believe that Fe elements extensively and mostly exist in the form of Fe_2N phase. Significantly, it is found that C and N elements evenly distribute in the whole matrix, manifesting the uniform doping of N elements into carbon skeletons. When getting rid of Fe_2N particles, there are C and N elements evenly locating all over the main matrix (Fig. 4d) along with slight Fe elements. In other words, Fe elements, in the Fe_2N@NC sample, exist dominantly in the form of Fe_2N crystal phases and scarcely coordinate with N atoms to form Fe-N_x sites.

The surface chemical composition and primary bonding configuration of Fe_2N@NC and AA-Fe_2N@NC sample were assessed by X-ray photoelectron spectroscopy (XPS). As expected, all the peaks of C, N, O and Fe elements are present in the survey spectrum of Fe_2N@NC sample (Fig. 5a), but for AA-Fe_2N@NC sample, the signal of Fe element is missing, supporting for the absence of Fe_2N particles, to some extent. It is widely accepted that carbon based materials contain two types of carbon atoms, the sp^2 carbon atoms at basal-plane and the sp^3 defect carbon atoms. Therefore, the defect degree of carbon materials is intimately relevant to the sp^3 carbon concentration [40,43]. The C 1s high-resolution spectrum can be de-convoluted into five peaks centered at 284.8, 285.9, 286.8, 287.8 and 289.5 eV, corresponding to basal-plane sp^2 carbon, sp^3 defect carbon, C–O bonds, C═O/C–N bonds and π-π* satellite peak, respectively [37,43]. Compared with Fe_2N@NC, the sp^3/sp^2 ratio of AA-Fe_2N@NC sample increases from 0.17 to 0.20 (Table S4, Supporting Information), and the relative concentration of sp^3 defect carbon in AA-Fe_2N@NC (14.08%) is also bigger than that of Fe_2N@NC (12.78%), indicative of the enhanced defective carbon content in AA-Fe_2N@NC [40], which is in accordance with the results of TEM observation and Raman spectra. In Fig. 5c, the binding energies at 398.5, 399.0, 399.8, 401.1 and 402.9 eV are assigned to pyridinic N, Fe-N compounds, pyrrolic N, graphitic N and oxidized N, respectively [34,44]. Notably, Fe-N compounds further make the existence of Fe_2N phase in Fe_2N@NC sample acceptable. What surprises us is that the relative concentration of pyridinic N in AA-Fe_2N@NC is as high as 37.8%, about 2.22 times large as that of Fe_2N@NC. More unlocked surface area induced by acid-washing treatment could possibly expose more C—N structures with various configurations or defects, and in our AA-Fe_2N@NC sample, pyridinic N acquires a priority to be released among these N-containing groups. Fortunately, pyridinic N has been identified as highly active sites to catalyze oxygen reduction reaction and is responsible for promoting electrocatalytic activities [45]. For Fe_2N@NC, the Fe 2p peak (Fig. 5d) can be divided into four parts: Fe $2p_{3/2}$, shake-up satellite peak, Fe $2p_{1/2}$ and shake-up satellite peak, locating at 710.9, 720.1, 724.7 and 733.2 eV, respectively [46]. Comparatively, the Fe 2p high-resolution spectrum curve is roughly flat and without obvious peaks, proving the removal of Fe_2N particles again. However, the XPS measurement is not enough sensitive to the element detection with extremely low concentration. In this regard, ICP-OES is employed to precisely figure out the content of Fe in the two samples. As-shown in Table S5 (Supporting Information), the relative mass concentrations of Fe element in Fe_2N@NC and AA-Fe_2N@NC sample are 52.3% and 0.94%, respectively, which means traces Fe distributing in doped carbon matrix. This measured values are different from the XPS results. It could be attributed to that XPS is related to the surface while ICP-OES is the reflection of overall bulk. Unfortunately, these

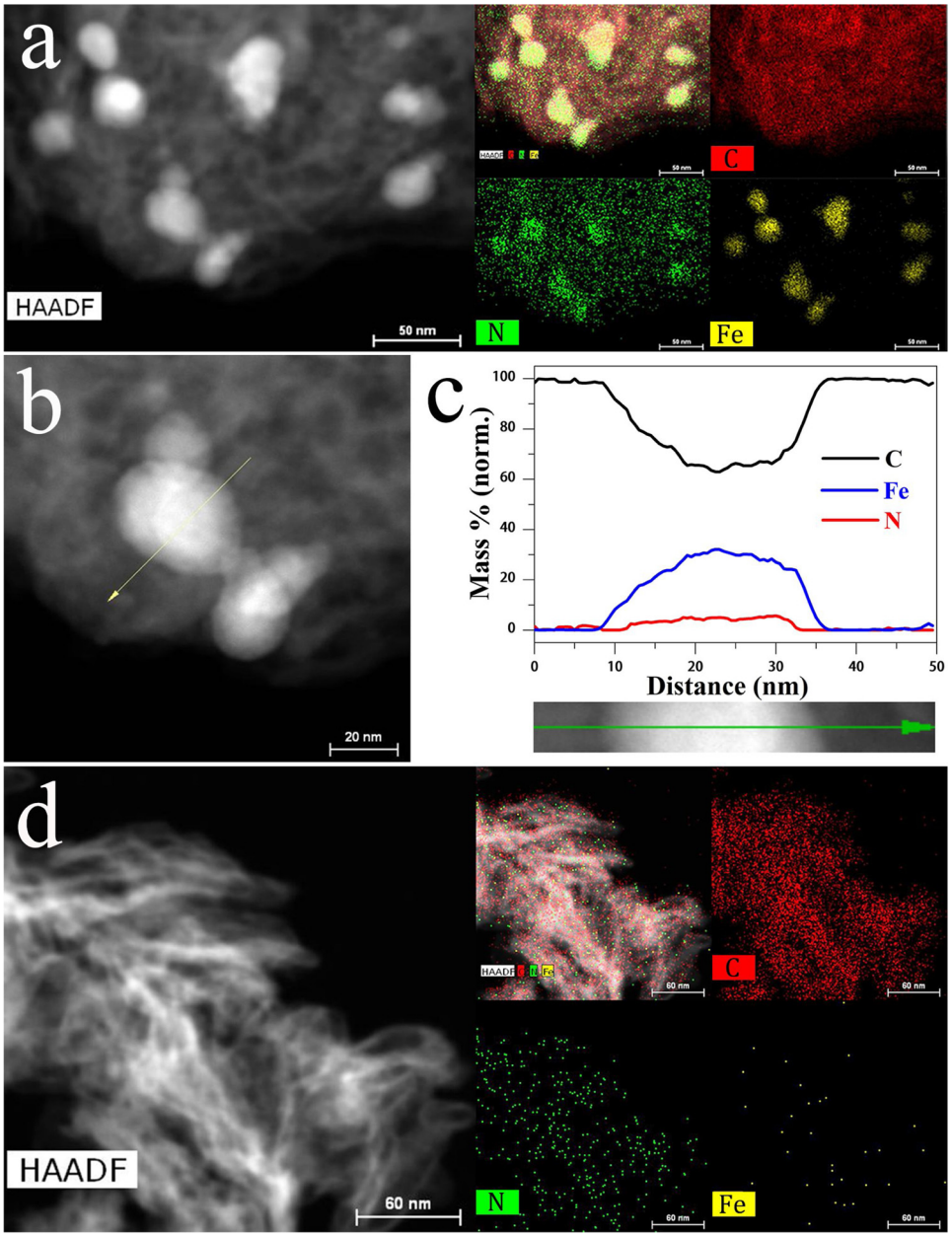

Fig. 4. A HAADF-STEM image and corresponding EDS mapping of C, N and Fe elements for Fe_2N@NC (**a**) and AA- Fe_2N@NC (**d**) sample. Elemental distributions of C, Fe and N elements for Fe_2N@NC sample in a single nanoparticle extracted from a STEM–EELS line profile (**b** and **c**).

Fe_2N nanoparticles are coated with several layer of carbon shells. In consideration of well-recognized surface processes of electrocatalysis, the XPS results could be accordingly acceptable.

As a powerful tool to identify the chemical states and atomic structure of Fe-species in as-fabricated Fe—N—C catalysts, ^{57}Fe Mössbauer spectra were performed and displayed in Fig. 6. The specific assignments of Fe-species according to the experimental Mössbauer parameters are summarized in Table S6 (Supporting Information). As revealed, the spectrum of Fe_2N@NC (Fig. 6a) could be fitted with four parts: two doublets (D1 and D2) and two sextets (Sextet 1 and Sextet 2). They are attributed to Fe_xN ($x \leq 2.1$, D1) [20,47], $Fe^{III}N_4$ site high-spin (D2) [47], $Fe_xC/Fe_2C_xN_{1-x}$ (Sextet 1) [48,49] and oxidized Fe particles (Sextet 2) [50], respectively. The sub-spectrum of Fe_xN ($x \leq 2.1$, D1) originates from inorganic Fe_2N nanoparticles. Similar with one previous work [50], the sextet 2 corresponding to oxidized Fe particles is probably caused by surface oxidization of Fe_2N particles. As for AA-Fe_2N@NC (Fig. 6b), only two doublets (D1′:$Fe^{III}N_4$ site high-spin state and D2′: $Fe^{II}N_4$ site low-spin state) [51,52] related to two kinds of Fe-N_4 sites could be deconvoluted. These Fe-N_4 structures are likely serving as active sites to catalyze for ORR. Obviously, inorganic Fe-involving nanoparticles in AA-Fe_2N@NC are not detected after acid-treatment of Fe_2N@NC sample, instead two types of organically coordinated Fe-N_4 sites are demonstrated. All these facts are consistent with above-mentioned other characterization results.

3.3. Electrochemical measurements analysis

According to the above analysis, as-obtained Fe—N—C samples are expected to develop as promising high-performance ORR catalysts. The ORR activities are preliminarily evaluated by CV measurements in N_2-saturated/O_2-saturated 0.1 M KOH electrolyte. For all samples, effective oxygen reduction processes could be revealed from the apparent reduction peaks in O_2-saturated rather than N_2-saturated electrolyte (Fig. 7a). The reduction peak current density of AA-Fe_2N@NC (1.07 mA

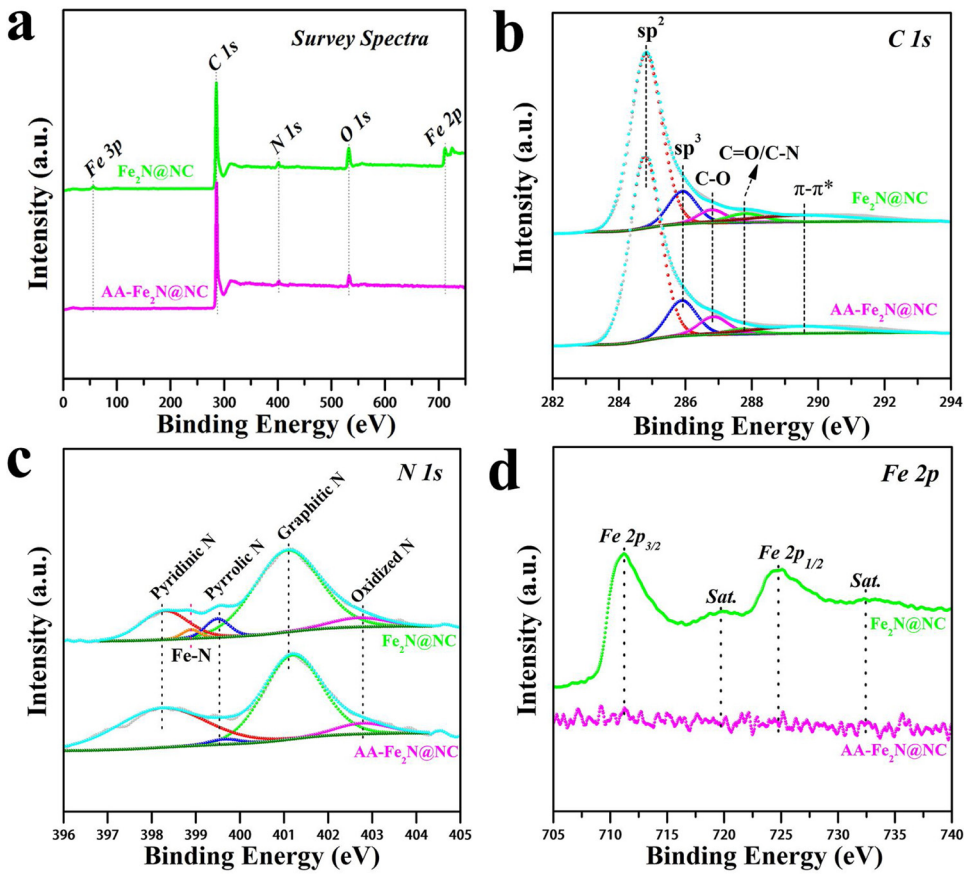

Fig. 5. XPS measurements of as-obtained Fe_2N@NC and AA-Fe_2N@NC sample. Survey spectra (**a**), High-resolution spectra of C 1s (**b**), N 1s (**c**) and Fe 2p (**d**).

cm^{-2}) sample at 50 mV s^{-1} is larger than that of Fe_2N@NC (0.74 mA cm^{-2}) sample and Pt/C catalyst (0.47 mA cm^{-2}), implying an inherently outstanding ORR activity of AA-Fe_2N@NC sample in alkaline electrolyte [53]. The prominent ORR activities of AA-Fe_2N@NC sample are further determined by linear sweep voltammetry (LSV) polarization curves (Fig. 7b). AA-Fe_2N@NC sample exhibits an onset potential (E_{onset}) of -0.073 V vs. Ag/AgCl (If not particular mention, the potential in this work is relative to Ag/AgCl electrode at 25 °C), a half-wave potential ($E_{1/2}$) of -0.172 V along with a limiting current density of 5.44 mA cm^{-2} in 0.1 M KOH electrolyte. All the properties are superior to those of Fe_2N@NC (E_{onset} = -0.145 V; $E_{1/2}$ = -0.217 V; j_L = 4.47 mA cm^{-2}) sample and Pt/C (E_{onset} = -0.065 V; $E_{1/2}$ = -0.228 V; j_L = 4.50 mA cm^{-2}) catalyst (Fig. 7e). More significantly, we find that, after removing Fe_2N nanoparticles in Fe_2N@NC sample, the overall ORR activities of AA-Fe_2N@NC sample are amazingly enhanced, which demonstrates that Fe_2N compounds are not dominating active sites, to a certain extent. The explicit ORR kinetics of AA-Fe_2N@NC sample could be disclosed by RDE measurements at various rotating rates (Fig. 7c). These LSV curves give a typical phenomenon that the current densities increase with the higher rotating rates because of the shortened gas diffusion distance [23]. In Fig.7d, the corresponding Koutecky–Levich (K–L) plots with good linearity and parallelism among the fitting lines at various potentials suggest a first-order reaction involved with the dissolved oxygen concentration [54]. Furthermore, the electron transfer number (n) of AA-Fe_2N@NC sample is calculated as 4.00 ~ 4.05 between -0.4 V and -0.8 V by using K–L formula, revealing a dominated four-electron transfer mechanism in ORR procedure [23]. The Tafel slope (Fig. 7f) of AA-Fe_2N@NC sample in low current density region is estimated to be 59 mV dec^{-1}, which is a little smaller than that of Fe_2N@NC sample (63 mV dec^{-1}) and Pt/C catalyst (87 mV dec^{-1}). This result sufficiently demonstrates a favorable kinetics mechanism towards ORR for AA-Fe_2N@NC sample, signifying that AA-Fe_2N@NC catalyst can

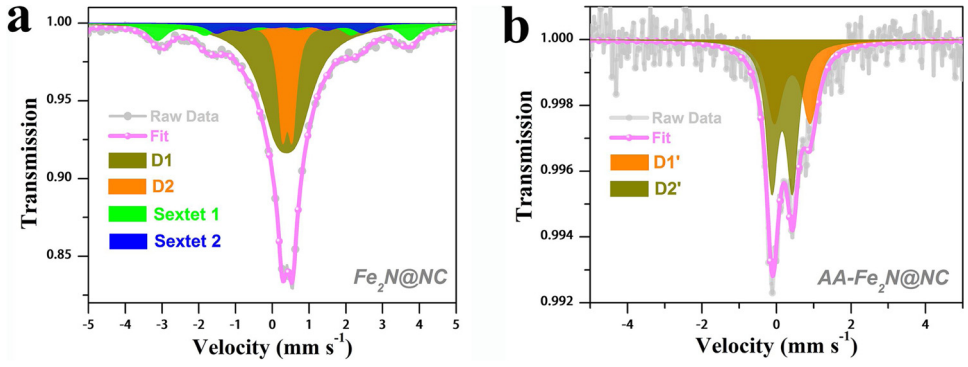

Fig. 6. ^{57}Fe Mössbauer spectra of Fe_2N@NC (**a**) and AA-Fe_2N@NC (**b**) sample measured at room temperature.

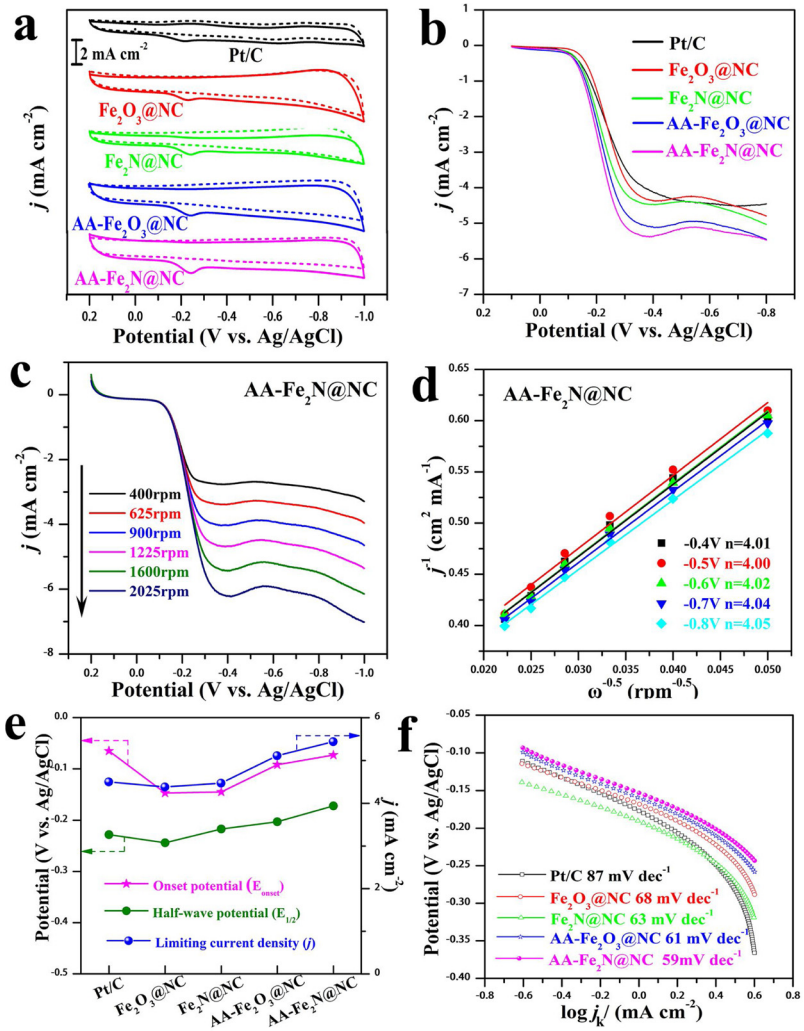

Fig. 7. Cyclic voltammetry (CV) at scan rate of 50 mV s^{-1} in 0.1 M KOH electrolyte (**a**). RDE measurements (LSV curves) in 0.1 M O_2-saturated (solid line) and N_2-saturated (dashed line) KOH electrolyte at 1600 rpm, scan rate: 10 mV s^{-1} (**b**). RDE measurements (**c**) at various rotation rates (scan rate: 10 mV s^{-1}) and corresponding K–L plots (**d**) of AA-Fe_2N@NC sample. The summary of E_{onset}, $E_{1/2}$ and j_L values (**e**). Tafel slopes of different samples (**f**).

reach higher current density at a lower overpotential [55].

To better understand the ORR catalytic activity, the mass activity and turnover frequency (TOF) of Fe_2N@NC and AA-Fe_2N@NC sample at the potential value of E^0 (E^0 is the value of half-wave potential for AA-Fe_2N@NC sample.) are calculated and presented in Table. 1. The mass activity of AA-Fe_2N@NC sample is 13.9 A g^{-1}, overmatching that of Fe_2N@NC sample. The intrinsic catalytic activities of the two samples are further assessed by TOF values. When assuming pyridinic N and defective carbon atoms as catalytically active sites, AA-Fe_2N@NC sample shows higher TOF value of 0.022 s^{-1} and 0.0038 s^{-1}, outperforming Fe_2N@NC sample. If taking Fe atoms as active centers, the corresponding TOF value for AA-Fe_2N@NC sample is as high as 0.209 s^{-1}. By contrast, the value for Fe_2N@NC sample just reach to 0.003 s^{-1}. However, this result could not actually prove that Fe-N_x groups are main active sites. It is because that, for Fe_2N@NC sample, the mass concentration of Fe is derived from overwhelming majority of Fe_2N compounds, while these Fe_2N particles might play minor role in catalytic reaction. In fact, it is hard to figure out the precise distribution of Fe elements in Fe_2N compounds and Fe-N_x groups as well as N elements in Fe_2N compounds and C–N_x groups. Based on this consideration, the role of Fe-N_x groups in our Fe—N—C system is necessary to be further probed by SCN^- inhibition studies.

Table 1
Comparison of electrocatalytic activity of various samples.

Samples	Mass activity at E^0 (A g^{-1})	TOF_{Fe} at E^0 (s^{-1})[a]	TOF_N at E^0 (s^{-1})[a]	TOF_{sp3C} at E^0 (s^{-1})[a]
Fe_2N@NC	11.0	0.003[b]	0.016	0.0034
AA-Fe_2N@NC	13.9	0.209	0.022	0.0038

Note: E^0 is the value of half-wave potential for AA-Fe_2N@NC sample.

[a] TOF values were evaluated by supposing that every corresponding atom are participated in the catalytic processes. (Details about the calculation are available from Supporting Information).

[b] Containing Fe atoms in Fe_2N nanocrystal and Fe-N_x groups.

On the other hand, durability and methanol-tolerance are considered as other key factors to evaluate the property of catalysts [52]. After the accelerated durability tests (ADT), we obtained the ORR polarization curves of AA-Fe_2N@NC sample and Pt/C catalyst (Fig. 8). Even sustaining CV test for 10,000 cycles, AA-Fe_2N@NC sample, analogous to other Fe—N—C samples (Fig. S11, Supporting Information), still show surprising stability with a half-wave potential drop of 1 mV, which is much smaller than that of Pt/C catalyst (13 mV negative shift). Besides, AA-Fe_2N@NC catalyst possesses commendable tolerance for methanol poisoning, exhibiting overlapped CV curves with/without the presence of 3 M methanol (Fig. 8c). This is completely different from Pt/C catalyst. After adding 3 M methanol into KOH electrolyte, a distinct oxidation peak appeared in the CV curve of Pt/C catalyst (Fig. 8d),

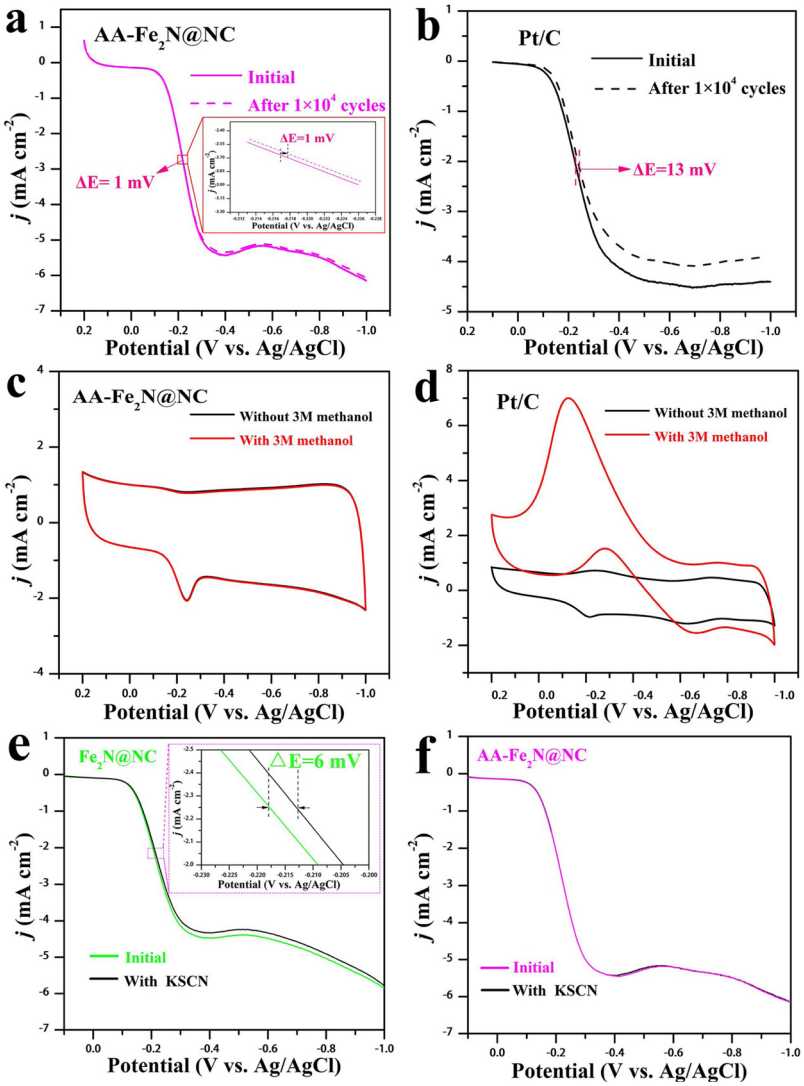

Fig. 8. ORR polarization curves of AA-Fe_2N@NCsample (**a**) and Pt/C catalyst (**b**) before and after 10,000 potential cycles; Methanol tolerance tests: CV curves of AA-Fe_2N@NC sample (**c**) and Pt/C catalyst (**d**) with and without injecting 3 M methanol into O_2-saturated electrolyte; ORR polarization curves of Fe_2N@NC (**e**) and AA-Fe_2N@NC (**f**) sample before and after soaked in 5 mM KSCN solution.

identifying the existence of methanol oxidation reaction. The high methanol tolerance means that AA-Fe_2N@NC catalyst is a promising candidates for electrode material used in fuel cells.

For purpose of investigating the role of Fe-based species in Fe_2N@NC sample for ORR, we employed SCN^- ion as an ORR active site inhibitor. As we know, SCN^- ions are prone to coordinate with surface iron ions and consequently reducing ORR activity if Fe-based groups are main active sites [16,26]. After soaking in 0.1 M KOH electrolyte with 5 mM KSCN for 2 h, the ORR half-wave potential of Fe_2N@NC sample (Fig. 8e) only decreases by 6 mV, which means that Fe_2N phases and Fe-N_x groups in Fe_2N@NC sample are not main active sites for ORR. As shown in Fig. 8f, AA-Fe_2N@NC sample maintains the same ORR activities, whatever poisoned by SCN^- ions or not. This is because that active sites including C–N groups and carbon defects are almost immune to the toxicant effect of SCN^- ions, simultaneously further verifying that Fe-N_x groups don't serve as the primary active sites towards ORR. All the above results approve that, for these Fe—N—C catalysts, N-containing groups and defective carbon structures rather than Fe_2N phases or Fe-N_x groups are dominant ORR active sites and responsible for the enhanced ORR performances.

3.4. Rechargeable Zn-air battery

To further probe the satisfactory catalytic activity and durability, a rechargeable home-made Zn-air battery (Fig. 9a) was fabricated by using as-prepared AA-Fe_2N@NC sample as catalyst cathode. For comparison, a mixture of commercial Pt/C and RuO_2 catalysts (Pt/C-RuO_2) with a mass ratio of 1:1 was also made as air cathode. At room temperature, an open-circuit voltage of 1.49 V (Fig. 9b) could be achieved for as-assembled AA-Fe_2N@NC air battery, slightly higher than that of Pt/C-RuO_2 (1.47 V). With a scan rate of 5 mV s^{-2}, we measured the polarization (V-j) curves of Zn-air batteries made from various catalyst air cathodes. The V-j curves and corresponding power density plots are exhibited in Fig. 9c. As-observed, the AA-Fe_2N@NC sample affords a larger power density of 168.15 mW cm^{-2} and a higher current density of 300 mA cm^{-2} at 0.54 V, which surpass those of Fe_2N@NC sample (134.02 mW cm^{-2} and 248 mA cm^{-2}), Pt/C-RuO_2 catalyst (141.48 mW cm^{-2} and 262 mA cm^{-2}) and some other reports [27,56,57]. These facts demonstrate superior catalytic activity of AA-Fe_2N@NC sample. The long-term rechargeability (Fig. 9d) of as-made Zn-air battery, the cycling tests were carried out at a constant density of 5 mA cm^{-2} (charging for 10 min and discharging for 10 min). In the beginning, the battery fabricated with AA-Fe_2N@NC catalyst exhibits a discharging

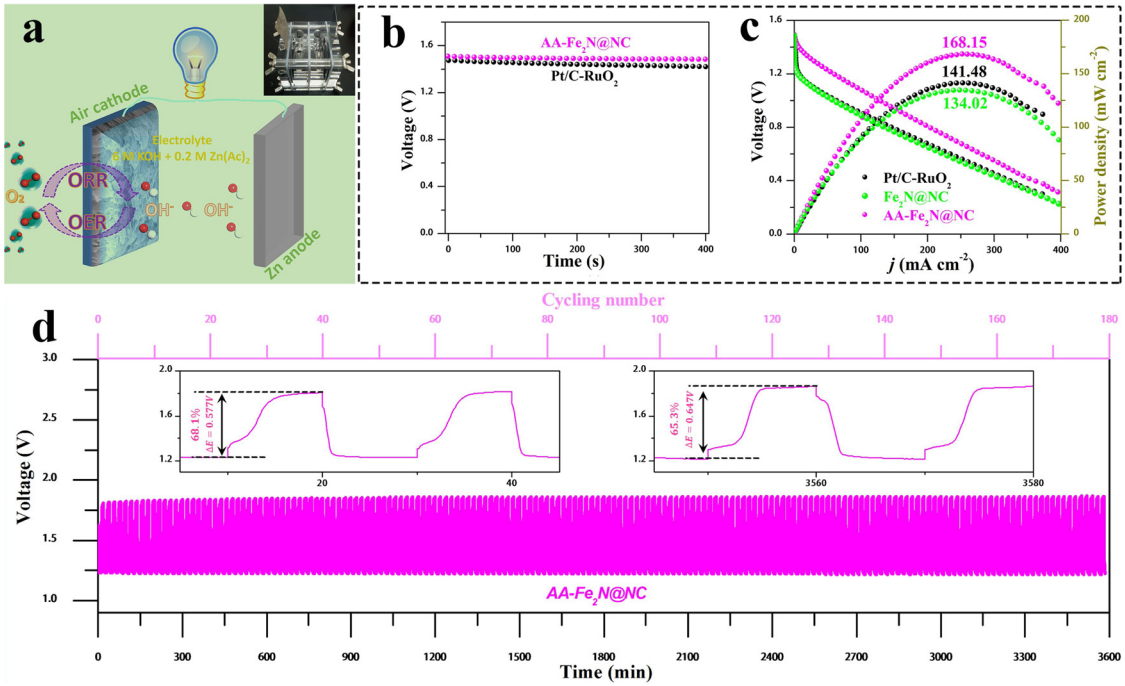

Fig. 9. Schematic illustration of home-made rechargeable Zn-air battery (**a**); Open-circuit voltage (**b**), polarization and power density curves (**c**) of Zn-air batteries assembled with various catalysts air cathodes; Galvanostatic discharging and charging cycling curves of the Zn-air battery with AA-Fe_2N@NC air cathode at a current of 5 mA cm^{-2} for 10 min discharge and 10 min charge (**d**).

voltage of 1.231 V and a charging voltage of 1.808 V, with a relatively small voltage gap of 0.577 V and a high onset round-trip efficiency of 68.1%, which are even better than the values reported [58]. After continuous cycling operation for about 60 h (180 cycles), the voltage gap only increases about 70 mV, demonstrating the excellent stability for AA-Fe_2N@NC air cathode.

3.5. Discussion and summary about active sites

Based on the aforementioned structure, component and property characterizations, some discussions are necessary to take for preferably understanding the dominant ORR active sites. Derived from g-C_3N_4/$FeC_2O_4{\cdot}2H_2O$ composite, we, as expected, fabricate graphitic carbon wrapped Fe_2O_3 nanoparticles and metallic Fe decorated nitrogen doped carbon hybrids (Fe_2O_3@NC). By means of acid-washing treatment, the surface area and pore volume of AA-Fe_2O_3@NC sample are accordingly increased on account of the removal of fractional metallic Fe and Fe_2O_3 particles, but most of Fe-containing species are still residual in carbon matrixes. Reacting with NH_3 at high temperature, both metallic Fe and Fe_2O_3 particles enable to transform to be Fe_2N compounds, meanwhile it is observed by HRTEM images (Fig. 2h) that the graphitic carbon shells encircled Fe_2N particles become discontinuous and broken in as-developed Fe_2N@NC sample, during the process of acid-washing treatment. This fact facilitates the diffusion of H^+ ions into the interior of graphitic carbon shells, and then eliminating Fe_2N particles as much as possible to acquire AA-Fe_2N@NC sample. In fact, trace Fe-specie rather than Fe_2N phase is detectable in AA-Fe_2N@NC sample, according to XRD, SEM, TEM, EDS mapping, XPS, ICP-OES and Mössbauer spectra results. The trace Fe-species are demonstrated existing in the form of two different Fe-N_4 sites. Of great significance, it is confirmed by HRTEM image, Raman and XPS spectra that AA-Fe_2N@NC sample has more abundant carbon defects and pyridinic N concentration in comparison to Fe_2N@NC sample. As a consequence, AA-Fe_2N@NC sample exhibits better overall ORR performances than Fe_2N@NC sample with a E_{onset} of -0.073 V, a $E_{1/2}$ of – 0.172 V, a j_L of 5.44 mA cm^{-2} and a Tafel slope of 59 mV dec^{-1}, even surpassing commercial 20 wt% Pt/C catalyst. In addition to those, AA-Fe_2N@NC catalyst is also demonstrated to be highly active and stable air cathode for rechargeable Zn-Air battery. By right of a SCN^- ions poisoning experiment (Fig. 8), it is reasonably believed that, for this Fe—N—C system, N-containing groups and carbon defects are primary ORR active sites, while Fe_2N phases and Fe-N_x groups play a minor role in catalyzing for ORR.

4. Conclusions

In summary, we have successfully converted Fe/Fe_2O_3 species into Fe_2N compounds and simultaneously broken the graphitic carbon shells peripheral to these particles by using a surface engineering process, which facilitates the diffusion of H^+ ions and makes it easier to completely remove Fe_2N particles. It is confirmed by various techniques that Fe elements of Fe_2N@NC sample exist in the form of Fe_2N nanocrystals and fairly slight Fe-N_x groups. After eliminating these Fe_2N particles, Raman and XPS spectra show that I_D/I_G and sp^3/sp^2 carbon values of AA-Fe_2N@NC sample are increased to 1.35 and 0.20 from 1.07 and 0.17 of Fe_2N@NC sample, respectively, suggesting an enhanced defective carbon concentration. Additionally, the relative concentration of pyridinic N in N 1s for AA-Fe_2N@NC sample reaches up to 37.8%, around 2.2 times big as that of Fe_2N@NC sample. Consequently, AA-Fe_2N@NC sample shows much superior catalytic performances than Fe_2N@NC, with more positive onset potential (72 mV positive shift) and half-wave potential (45 mV positive shift), as well as a smaller Tafel slop (59 mV dec^{-1}), consistent with the corresponding TOF values. It surprisingly affords a high power density of 168.15 mW cm^{-2}, a relatively small voltage gap of 0.577 V and a high onset round-trip efficiency of 68.1% when used as air cathode for liquid Zn-air battery. Combined with SCN^- inhibition experiment result, it is proposed and highlighted that, for this Fe—N—C system, carbon defects and C—N structures (pyridinic N) rather than Fe_2N compounds and Fe-N_x groups, acting as dominated active sites, contribute to high-efficiency ORR activities in alkaline media. Hence, we emphasize that iron nitride compounds play minor role in catalyzing for ORR, but could give rise to a satisfactory ORR property as well if one develops an effective surface

modification strategy to release more non-metal active sites.

Conflicts of interest

There are no conflicts of interests to declare.

Acknowledgement

We greatly acknowledge the financial support of the National Natural Science Foundation of China (Grant No. 11674398).

Appendix A. Supplementary data

Supplementary material related to this article can be found, in the online version, at doi:https://doi.org/10.1016/j.apcatb.2019.05.037.

References

[1] M. Zhou, H.L. Wang, S. Guo, Chem. Soc. Rev. 45 (2016) 1273–1307.
[2] J. Masa, W. Xia, M. Muhler, W. Schuhmann, Angew. Chem. Int. Ed. 54 (2015) 10102–10120.
[3] M. Shen, C. Wei, K. Ai, L. Lu, Nano Res. 10 (2017) 1449–1470.
[4] G. Wu, A. Santandreu, W. Kellogg, S. Gupta, O. Ogoke, H. Zhang, H.-L. Wang, L. Dai, Nano Energy 29 (2016) 83–110.
[5] T. Varga, L. Vásárhelyi, G. Ballai, H. Haspel, A. Oszkó, Á. Kukovecz, Z. Kónya, ACS Omega 4 (2019) 130–139.
[6] T. Asefa, Acc. Chem. Res. 49 (2016) 1873–1883.
[7] X. Wang, B. Wang, J. Zhong, F. Zhao, N. Han, W. Huang, M. Zeng, J. Fan, Y. Li, Nano Res. 9 (2016) 1497–1506.
[8] A.A. Gewirth, J.A. Varnell, A.M. DiAscro, Chem. Rev. 118 (2018) 2313–2339.
[9] W.J. Jiang, L. Gu, L. Li, Y. Zhang, X. Zhang, L.J. Zhang, J.Q. Wang, J.S. Hu, Z. Wei, L.J. Wan, J. Am. Chem. Soc. 138 (2016) 3570–3578.
[10] C.V. Rao, C.R. Cabrera, Y. Ishikawa, J. Phys. Chem. Lett. 1 (2010) 2622–2627.
[11] J. Zhang, Y. Sun, J. Zhu, Z. Kou, P. Hu, L. Liu, S. Li, S. Mu, Y. Huang, Nano Energy 52 (2018) 307–314.
[12] A. Zhu, L. Qiao, P. Tan, W. Zeng, Y. Ma, R. Dong, J. Pan, J. Colloid Interface Sci. 541 (2019) 133–142.
[13] L. Qiao, A. Zhu, H. Yang, W. Zeng, R. Dong, P. Tan, D. Zhong, Q. Ma, J. Pan, Inorg. Chem. Front. 5 (2018) 2276–2283.
[14] M. Wu, K. Wang, M. Yi, Y. Tong, Y. Wang, S. Song, ACS Catal. 7 (2017) 6082–6088.
[15] A. Zitolo, V. Goellner, V. Armel, M.T. Sougrati, T. Mineva, L. Stievano, E. Fonda, F. Jaouen, Nat. Mater. 14 (2015) 937–942.
[16] W. Niu, L. Li, X. Liu, N. Wang, J. Liu, W. Zhou, Z. Tang, S. Chen, J. Am. Chem. Soc. 137 (2015) 5555–5562.
[17] C. Zhu, H. Li, S. Fu, D. Du, Y. Lin, Chem. Soc. Rev. 45 (2016) 517–531.
[18] T. Sun, B. Tian, J. Lu, C. Su, J. Mater. Chem. A 5 (2017) 18933–18950.
[19] K. Strickland, E. Miner, Q. Jia, U. Tylus, N. Ramaswamy, W. Liang, M.T. Sougrati, F. Jaouen, S. Mukerjee, Nat. Commun. 6 (2015) 7343.
[20] M. Wang, Y. Yang, X. Liu, Z. Pu, Z. Kou, P. Zhu, S. Mu, Nanoscale 9 (2017) 7641–7649.
[21] J. Wang, H. Wu, D. Gao, S. Miao, G. Wang, X. Bao, Nano Energy 13 (2015) 387–396.
[22] Y. Deng, Y. Dong, G. Wang, K. Sun, X. Shi, L. Zheng, X. Li, S. Liao, ACS Appl. Mater. Interfaces 9 (2017) 9699–9709.
[23] A. Zhu, P. Tan, L. Qiao, Y. Liu, Y. Ma, X. Xiong, J. Pan, Inorg. Chem. Front. 4 (2017) 1748–1756.
[24] L.T. Song, Z.Y. Wu, F. Zhou, H.W. Liang, Z.Y. Yu, S.H. Yu, Small 12 (2016) 6398–6406.
[25] Q. Wang, Z.Y. Zhou, Y.J. Lai, Y. You, J.G. Liu, X.L. Wu, E. Terefe, C. Chen, L. Song, M. Rauf, N. Tian, S.G. Sun, J. Am. Chem. Soc. 136 (2014) 10882–10885.
[26] J. Liu, X. Sun, P. Song, Y. Zhang, W. Xing, W. Xu, Adv. Mater. 25 (2013) 6879–6883.
[27] W. Wan, X. Liu, H. Li, X. Peng, D. Xi, J. Luo, Appl. Catal. B: Environ. 240 (2019) 193–200.
[28] H. Yu, L. Shang, T. Bian, R. Shi, G.I. Waterhouse, Y. Zhao, C. Zhou, L.Z. Wu, C.H. Tung, T. Zhang, Adv. Mater. 28 (2016) 5080–5086.
[29] A. Zhu, L. Qiao, Z. Jia, P. Tan, Y. Liu, Y. Ma, J. Pan, Dalton Trans. 46 (2017) 17032–17040.
[30] Y. Li, W. Zhou, H. Wang, L. Xie, Y. Liang, F. Wei, J.C. Idrobo, S.J. Pennycook, H. Dai, Nat. Nanotechnol. 7 (2012) 394–400.
[31] J. Zhang, Y. Song, M. Kopec, J. Lee, Z. Wang, S. Liu, J. Yan, R. Yuan, T. Kowalewski, M.R. Bockstaller, K. Matyjaszewski, J. Am. Chem. Soc. 139 (2017) 12931–12934.
[32] M.-Q. Wang, C. Ye, M. Wang, T.-H. Li, Y.-N. Yu, S.-J. Bao, Energy Storage Mater. 11 (2018) 112–117.
[33] V.A. Setyowati, H.-C. Huang, C.-C. Liu, C.-H. Wang, Electrochim. Acta 211 (2016) 933–940.
[34] X. Huang, Z. Yang, B. Dong, Y. Wang, T. Tang, Y. Hou, Nanoscale 9 (2017) 8102–8106.
[35] M.-S. Balogun, M. Yu, Y. Huang, C. Li, P. Fang, Y. Liu, X. Lu, Y. Tong, Nano Energy 11 (2015) 348–355.
[36] J. Xiao, Y. Xu, Y. Xia, J. Xi, S. Wang, Nano Energy 24 (2016) 121–129.
[37] H.-F. Wang, C. Tang, B. Wang, B.-Q. Li, X. Cui, Q. Zhang, Energy Storage Mater. 15 (2018) 124–130.
[38] K. Mamtani, D. Jain, D. Dogu, V. Gustin, S. Gunduz, A.C. Co, U.S. Ozkan, Appl. Catal. B: Environ. 220 (2018) 88–97.
[39] Y. Wang, L. Tao, Z. Xiao, R. Chen, Z. Jiang, S. Wang, Adv. Funct. Mater. (2018) 1705356.
[40] L. Tao, Q. Wang, S. Dou, Z. Ma, J. Huo, S. Wang, L. Dai, Chem. Commun. 52 (2016) 2764–2767.
[41] L. Wang, J. Yin, L. Zhao, C. Tian, P. Yu, J. Wang, H. Fu, Chem. Commun. 49 (2013) 3022–3024.
[42] K. Wan, G.-F. Long, M.-Y. Liu, L. Du, Z.-X. Liang, P. Tsiakaras, Appl. Catal. B: Environ. 165 (2015) 566–571.
[43] Z. Liu, Z. Zhao, Y. Wang, S. Dou, D. Yan, D. Liu, Z. Xia, S. Wang, Adv. Mater. 29 (2017) 1606207.
[44] Y. Wang, H. Liu, K. Wang, S. Song, P. Tsiakaras, Appl. Catal. B: Environ. 210 (2017) 57–66.
[45] X. Cui, S. Yang, X. Yan, J. Leng, S. Shuang, P.M. Ajayan, Z. Zhang, Adv. Funct. Mater. 26 (2016) 5708–5717.
[46] Y. Li, J. Xu, T. Feng, Q. Yao, J. Xie, H. Xia, Adv. Funct. Mater. 27 (2017) 1606728.
[47] U.I. Kramm, M. Lefevre, N. Larouche, D. Schmeisser, J.P. Dodelet, J. Am. Chem. Soc. 136 (2014) 978–985.
[48] J.A. Varnell, J.S. Sotiropoulos, T.M. Brown, K. Subedi, R.T. Haasch, C.E. Schulz, A.A. Gewirth, ACS Energy Lett. 3 (2018) 823–828.
[49] Z. Yang, S. Guo, X. Pan, J. Wang, X. Bao, Energy Environ. Sci. 4 (2011) 4500–4503.
[50] N.R. Sahraie, U.I. Kramm, J. Steinberg, Y. Zhang, A. Thomas, T. Reier, J.P. Paraknowitsch, P. Strasser, Nat. Commun. 6 (2015) 8618.
[51] J. Li, S. Ghoshal, W. Liang, M.-T. Sougrati, F. Jaouen, B. Halevi, S. McKinney, G. McCool, C. Ma, X. Yuan, Z.-F. Ma, S. Mukerjee, Q. Jia, Energy Environ. Sci. 9 (2016) 2418–2432.
[52] Y.J. Sa, D.J. Seo, J. Woo, J.T. Lim, J.Y. Cheon, S.Y. Yang, J.M. Lee, D. Kang, T.J. Shin, H.S. Shin, H.Y. Jeong, C.S. Kim, M.G. Kim, T.Y. Kim, S.H. Joo, J. Am. Chem. Soc. 138 (2016) 15046–15056.
[53] Z. Pei, H. Li, Y. Huang, Q. Xue, Y. Huang, M. Zhu, Z. Wang, C. Zhi, Energy Environ. Sci. 10 (2017) 742–749.
[54] I.-A. Choi, D.-H. Kwak, S.-B. Han, J.-Y. Park, H.-S. Park, K.-B. Ma, D.-H. Kim, J.-E. Won, K.-W. Park, Appl. Catal. B: Environ. 211 (2017) 235–244.
[55] T. Zhou, Y. Du, S. Yin, X. Tian, H. Yang, X. Wang, B. Liu, H. Zheng, S. Qiao, R. Xu, Energy Environ. Sci. 9 (2016) 2563–2570.
[56] C. Li, H. Liu, Z. Yu, Appl. Catal. B: Environ. 241 (2019) 95–103.
[57] C. Li, M. Wu, R. Liu, Appl. Catal. B: Environ. 244 (2019) 150–158.
[58] H. Jiang, Y. Liu, W. Li, J. Li, Small 14 (2018) 1703739.